Observing the RM Effect using CYCLOPS

Brett Addison (b.addison@student.unsw.edu.au)

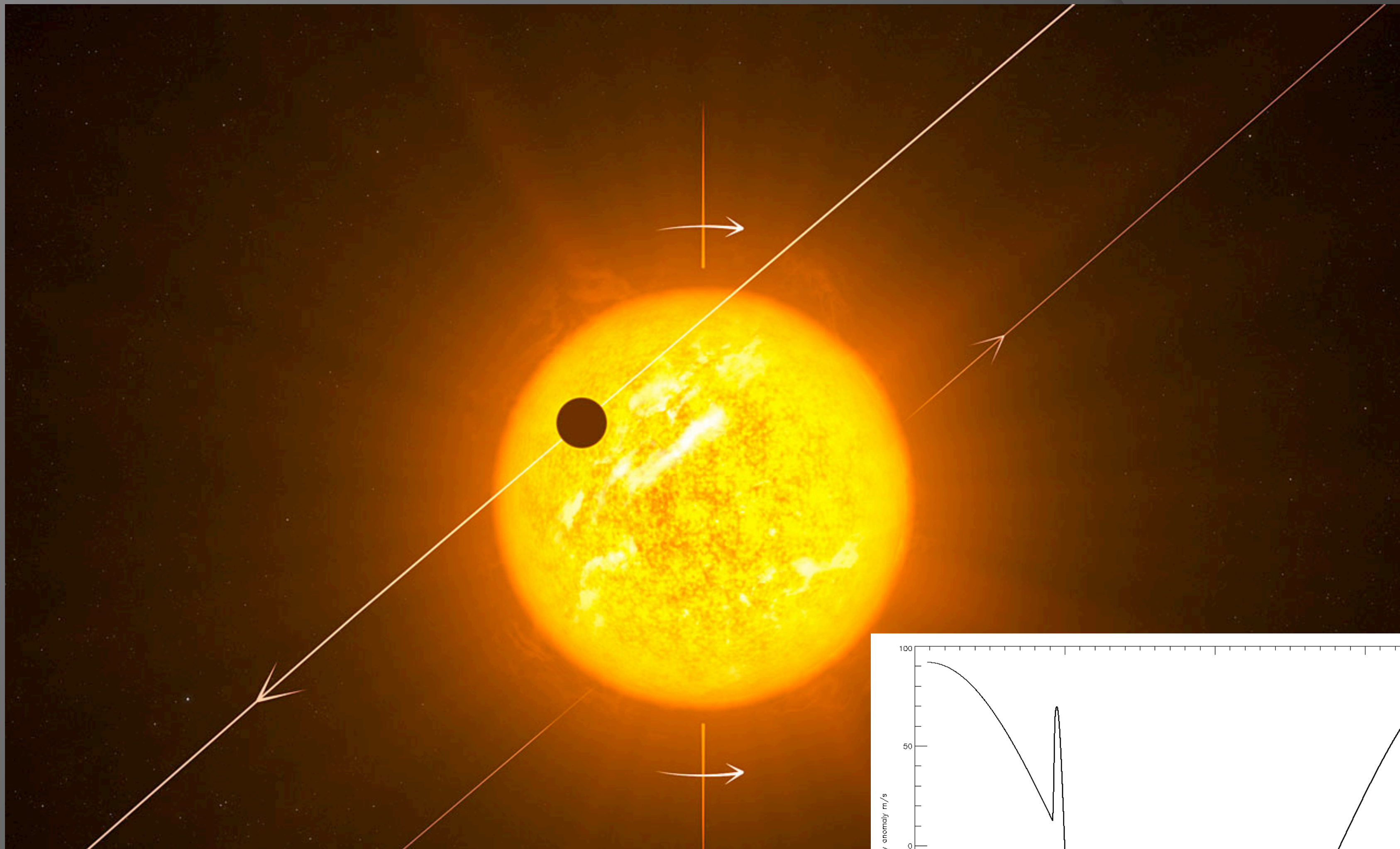

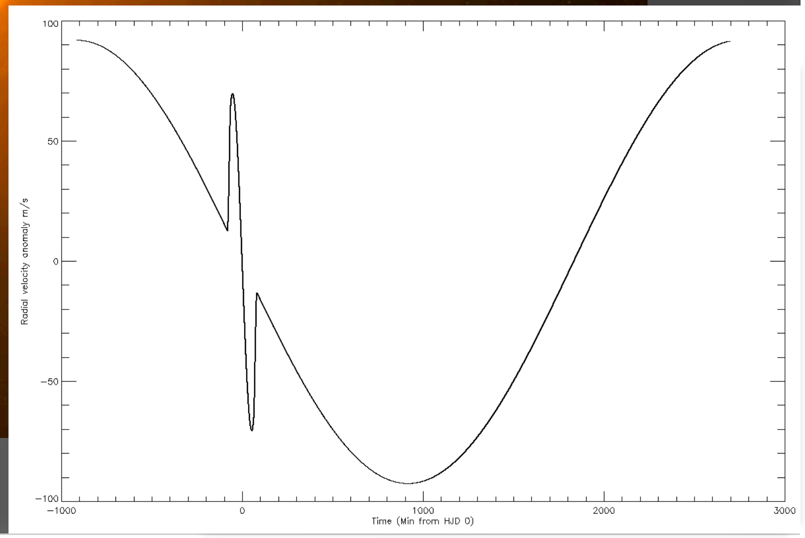

University of New South Wales, Sydney, Australia

GIANT PLANET DISRUPTIONS AND THEIR EFFECT ON THEIR HOST STARS

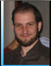

James Guillochon
UC Santa Cruz

Abstract: Driven by dynamical processes shortly after the protoplanetary disk dissipates, giant planets can often find themselves on orbits that approach so close to their parent stars that they are disrupted. Prior work has only focused on a planet's first passage. We present 3D hydrodynamical simulations of giant planet disruptions that occur over several orbits. The inclusion of these events greatly increases the amount of mass acquired by the host stars from planetary disruptions, and can produce the observed mis-alignment between the star's rotation axis and remaining planets within the system.

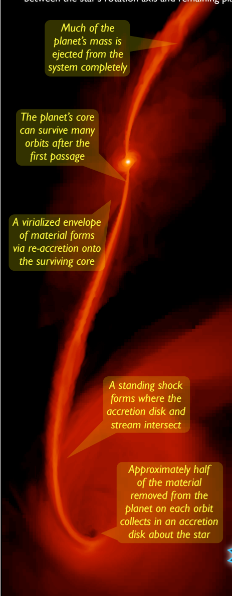

Much of the planet's mass is ejected from the system completely

The planet's core can survive many orbits after the first passage

A virialized envelope of material forms via re-accretion onto the surviving core

A standing shock forms where the accretion disk and stream intersect

Approximately half of the material removed from the planet on each orbit collects in an accretion disk about the star

For more details, see Guillochon et. al 2010 (arXiv: 1012.2382)

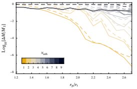

Figure 1. Mass loss history of multiple passage encounters for different initial values of r_p. Each curve is color-coded to correspond to a particular orbit number. The solid lines show the aggregate mass accreted by the star, while the dashed lines show the total mass lost from the planet.

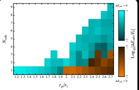

Figure 2. Change in orbital energy $E_{\rm orb}$ attributed to each passage as a function of r_p and orbit number $N_{\rm orb}$. The orange regions show decreases in $E_{\rm orb}$ (more bound), while the cyan regions show increases in $E_{\rm orb}$ (less bound). The height of each column shows the number of orbits a planet survives before being destroyed.

$$\Delta M_*(0.37 \le \beta \le 0.83) = \begin{cases} 1.26 \exp\left[-0.79\beta^{-1}\right] M_{\rm J} & : a_0 \ll a_{\rm ice} \\ 9.62 \exp\left[-2.59\beta^{-1}\right] M_{\rm J} & : a_0 \sim a_{\rm ice} \end{cases} \quad (1)$$

A fit to the expected amount of mass that remains bound to the star after a multi-orbit disruption of a Jupiter-mass planet, where $\beta \equiv R_{\rm P}\,(M_*/M_{\rm P})^{1/3}$. If the planet is scattered from the ice line ($a_{\rm ice}$), its orbital energy is so small that the planet becomes unbound as soon as $\Delta E_{\rm orb} > 0$ (see Figure 2), meaning the planet is ejected from the system prior to being completely destroyed. However, if the planet is scattered in from a distance where $E_{\rm orb} \sim GM_{\rm P}^2/R_{\rm P}^2$, the planet is destroyed prior to being ejected, and up to 40% of the planet's initial mass remains bound to the star.

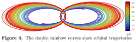

Figure 3. The double rainbow curves show orbital trajectories for both the planet (left) and star (right) during the encounter for different values of the periastron distance r_p. The star's trajectory is magnified by a factor of $M_*/M_{\rm P} = 10^3$ to make its motion apparent. While the orbits do precess slightly over the course of the simulations, this plot shows the orbits with the precession removed. Note that the $r_p = 2.1$ run (light green) experiences a particularly ejective encounter on its 2nd periastron passage.

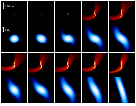

Figure 4. Slices through the orbital plane shortly after each periastron passage for the simulation where $r_p = 2.7r_t$. All plots show log ρ. The upper, red color-coded figures show a wide view of each encounter, with white corresponding to $\rho = 10^{-2}$ g cm^{-3} and black corresponding to $\rho = 10^{-7}$ g cm^{-3}, while the lower, blue color-coded figures show a close-up view of the core, with white corresponding to the maximum density $\rho_{\rm max}$ and black corresponding to $\rho = 10^{-2}$ g cm^{-3}.

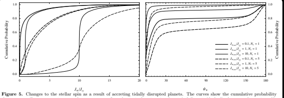

Figure 5. Changes to the stellar spin as a result of accreting tidally disrupted planets. The curves show the cumulative probability that a star will possess a given angular momentum J_* and spin inclination ψ_* after 1 (solid) or 5 (dashed) planetary disruptions $N_{\rm d}$ for different initial stellar angular momentum $J_{*,\rm init}$, with the amount of mass accreted ΔM_* being determined from an interpolation of Figure 1. Planets are assumed to have a logarithmic distribution in mass ($0.1M_{\rm J} \le M \le 10M_{\rm J}$) and semi-major axes ($r_\tau \le a \le 10a_{\rm ice}$), where r_τ is the minimum distance for which a planet won't be tidally disrupted and $a_{\rm ice}$ is the ice line. The eccentricity e and inclination i relative to the invariable plane are assumed to follow Rayleigh distributions, with $\sigma_e = 0.3$ and $\sigma_i = 10°$.

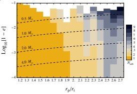

Figure 6. Criteria leading to planet ejection given an initial periastron passage distance r_p and eccentricity e. The colored regions correspond to the number of orbits before a planet is ejected by its interaction with the parent star. The dashed lines show the value of e given an apocenter distance equal to the ice line $a_{\rm ice}$, assuming that $L_* \propto M_*^{3.9}$. For all values of r_p shown and for $e \lesssim 0.97$, planets are ejected before they are totally disrupted.

Table 1

Planet	r_p/r_t	$r_{a,\rm max}/a_{\rm ice}$	$Q_{*,\rm max}$[a]	$\tau_{\rm life,max}$[a] (Gyr)
HAT-P-12 b	5.2	0.41	$1\times10^4 - 1\times10^5$	0.4 — 4
OGLE-TR-56 b	4.8	0.029	$2\times10^7 - 4\times10^7$	0.9 — 2
WASP-4 b	5.1	0.093	$5\times10^7 - 2\times10^8$	1 — 6
WASP-12 b	4.7	0.021	$5\times10^7 - 2\times10^8$	0.5 — 1
WASP-19 b	3.5	0.010	$2\times10^7 - 2\times10^8$	0.07 — 1

[a] Assuming $r_{p,0} = 2r_\tau$, $a_0 = a_{\rm ice}$. The minimum and maximum values are calculated using the lower and upper limits for $\tau_{\rm age}$ as compiled by Schlaufman et. al 2010.

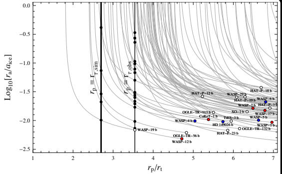

Figure 7. Possible apastrons r_a for the known hot Jupiters with $M_{\rm P} > 0.1M_{\rm J}$. Each arc shows the apocenter of an orbit with pericenter r_p, assuming that the angular momentum of the initial orbit is equal to the orbital angular momentum observed today. The open circles show each planet's currently observed r_p and r_a, scaled to the tidal radius r_t and the ice line $a_{\rm ice}$ respectively, which are determined by the planet/host star properties. Blue-filled circles are planets that are thought to be aligned with their host stars, red-filled circles are thought to be misaligned, and white-filled circles show systems with unknown orientations. The thick vertical line (labeled $r_{\tau,\rm sim}$) shows the minimum possible value of r_τ corresponding to the Jupiter exclusion zone, which is determined through our numerical simulations for Jupiter-like planets to be $2.7r_t$, while the thinner vertical line (labeled $r_{\tau,\rm obs}$) shows the maximum possible value for r_τ, which is defined by the planet that is currently observed to be closest to its classically defined tidal radius, WASP-19 b. Filled black circles show the intersection between the r_τ lines and each of the arcs of constant angular momentum shows the maximum apastron distance $r_{a,\rm max}$ a planet could have been scattered from without being destroyed on its subsequent encounters with the host star. Note that the typical $r_{a,\rm max}$ values are significantly smaller than $a_{\rm ice}$, which indicates that those planets must have migrated prior to being scattered if planet-planet scattering brought them to their current positions.

As the planet is likely to be tidally locked even prior to circularization, the timescale for evolution of the planet's semi-major axis is entirely determined by the star's properties and the orbital frequency ω (Dobbs-Dixon et. al 2004),

$$\frac{a}{\dot a} = \frac{1}{9} Q_* \left(\frac{M_*}{M_{\rm P}}\right)\left(\frac{a}{R_*}\right)^5 (\omega - \Omega_*)^{-1}, \quad (2)$$

where R_* is the star's radius, Q_* is the star's tidal quality factor, and Ω_* is its rotation frequency. The fastest inward migration occurs when a star is not rotating, e.g. $\Omega_* \to 0$. As planet-planet scattering seems to be rare after 10^8 yr (Matsumura et. al 2008), we can set $a/\dot a$ equal to the system age $\tau_{\rm age}$ to determine $Q_{*,\rm max}$, the maximum tidal quality factor for which a planet can migrate from $2r_\tau$ to $a_{\rm obs}$

$$Q_{*,\rm max} = 7\times10^5 \left(\frac{M_{\rm P}}{M_{\rm J}}\right)^{8/3}\left(\frac{M_*}{M_\odot}\right)^{-8/3}\left(\frac{R_{\rm P}}{R_{\rm J}}\right)^{-5}\left(\frac{r_\tau}{3r_t}\right)^{-5}\left(\frac{P_0}{3\ \rm days}\right)^{-1}\left(\frac{\tau_{\rm age}}{\rm Gyr}\right) \quad (3)$$

where P_0 is the initial orbital period. When setting $r_\tau = r_{\tau,\rm sim}$, all of the known hot Jupiters with $a_{\rm obs} < 2r_\tau$ yields values for $Q_{*,\rm max}$ that are consistent with those expected for stars (Table 1).

Extremely Metal-Poor stars and Formation of the Milky Way

<u>Y. Komiya (NAOJ)</u>
T. Suda, M. Y. Fujimoto
(Hokkaido Univ.)

EMP stars = relics from early universe.
They can be probes to …
- First stars,
- Galaxy formation,
- Individual characters of supernovae.

We build a chemical evolution model with *structure formation* & *high mass IMF*.

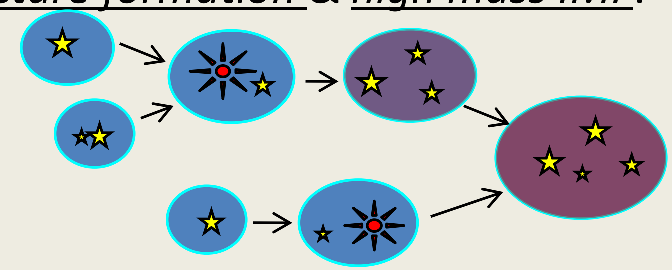

Metallicity distribution function

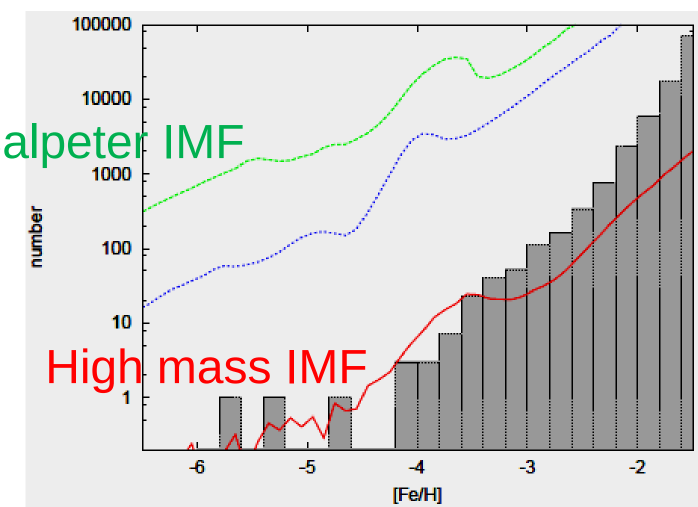

Abundance distribution

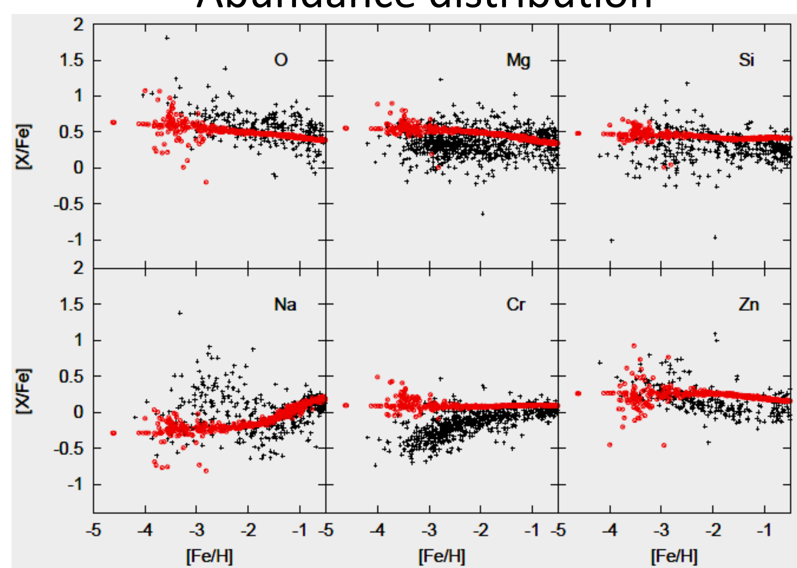

Gas Giant Formation with Small Cores Triggered by Envelope Pollution by Icy Planetesimals

Y. Hori & M. Ikoma

Dept. of Earth & Planetary Sciences, Tokyo Tech.

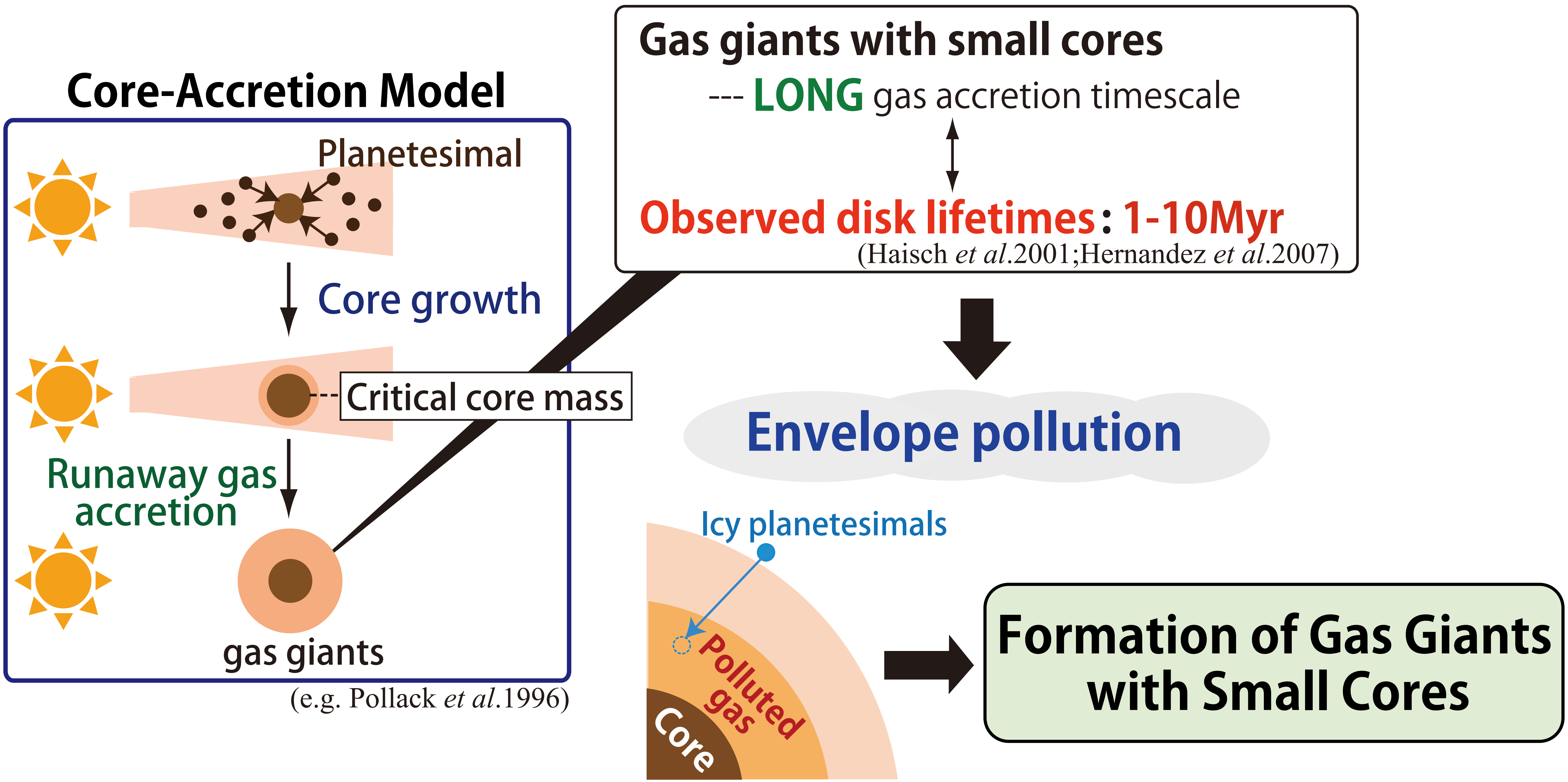

Formation of Dust Grains in the Ejecta of Type Ia Supernovae

Takaya Nozawa (IPMU, Univ. of Tokyo)
Keiichi Maeda, Takashi Kozasa, Masaomi Tanaka, Ken'ichi Nomoto, Hideyuki Umeda

Type Ia SN model : W7 model
Nomoto et al. (1984), Thilemann et al. (1986)

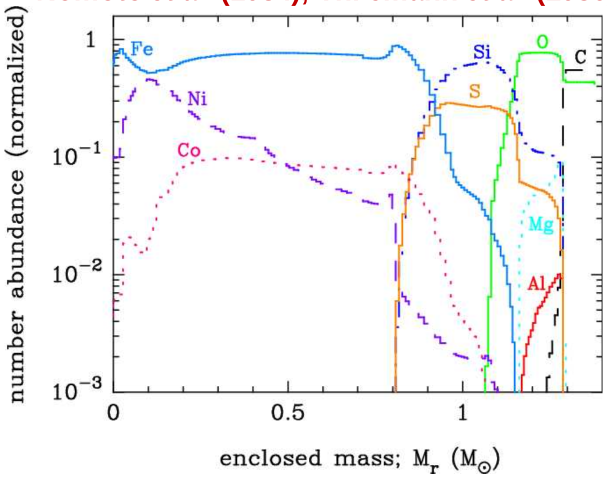

average radius of dust

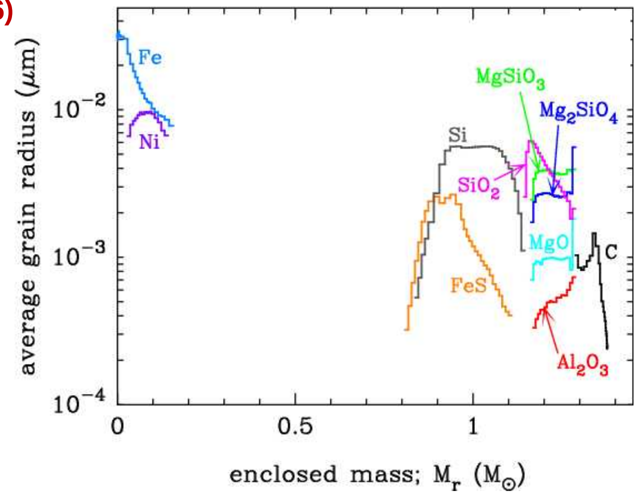

dust destruction in SNRs

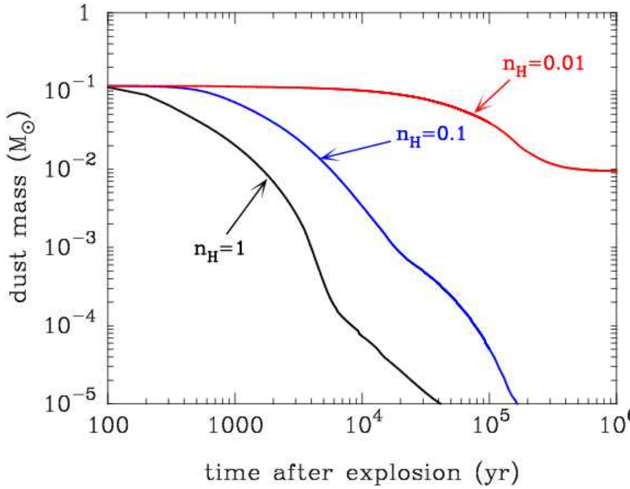

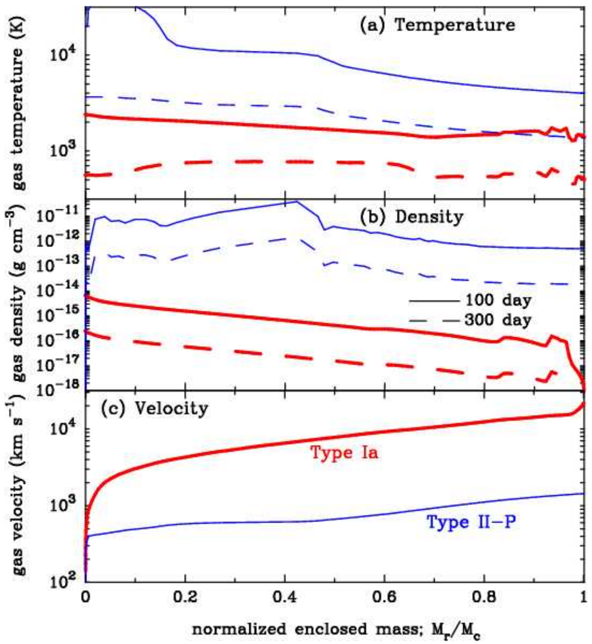

Results of dust formation calculation

- dust condensation time : **100-300 days**
- average radius of dust : a_{ave} <~ 0.01 μm
  (ref. a_{ave} >~ 0.1 μm for those in type II-P SNe)
- total dust mass : M_{dust} = 0.1-0.2 M_{sun}

Destruction of dust by the reverse shock in SNRs

- newly formed grains are almost completely destroyed for the ISM density of n_H > 0.1 cm^{-3}

➔ **SNe Ia are unlikely to be major sources of dust**

Detailed Radiative Transfer Schemes
in the 3-D Hydrodynamical Solar Surface

K. Bach & Y.-C. Kim

Yonsei University, Seoul, Korea

ABSTRACT. We have investigated the detailed non-grey radiative transfer scheme in the three dimensional hydrodynamical solar surface. Outer convection zone is extremely turbulent region composed of partly ionized compressible gases in high temperature. Especially, super-adiabatic layer (SAL) is the transition region where the transport of energy changes drastically from convection to radiation. In order to describe physical processes in SAL accurately, a realistic treatment of radiation should be considered as well as convection. For a detailed computation of radiative transfer, the Accelerated Lambda Iteration (ALI) methods have been applied to Large-Eddy Simulation (LES) with non-grey opacity schemes using the Opacity Distribution Function (ODF). Our computational domain is the rectangular box of dimensions $4^2 \times 3$ Mm with the resolution of $117^2 \times 190$ meshed grids, which covers several granules horizontally and 8~9 pressure scale heights vertically. As the result of numerical simulation, we present the time-dependent variation of radiation fields and thermodynamic structures in the solar outer convection zone. In addition, our radiation-hydrodynamical computation has been compared with the classical approximations such as grey atmosphere and Eddington approximation.

Solar Calibration

Initial Configuration The starting model for the 3-D simulation has been obtained using the 1-D stellar structure & evolution code, **YREC**. With well-defined observables such as solar effective temperature and luminosity, solar calibration is to find modeling parameter set. In this study, the standard solar model has been constructed based on the GS98 solar abundance.

Parameters	Values
(X_0, Y_0, Z_0)	(0.7085, 0.2726, 0.0188)
(X_s, Y_s, Z_s)	(0.7399, 0.2432, 0.0169)
$(Z/X)_\odot$	0.02292 (GS98)
α_{MLT}	1.87
Age	45.5 Gyr
Input microphysics	
Microscopic Diffusion	*Y, Z*–diffusion
Atmospheric approximation	Eddington T – τ
Solar mixture	Grevesse & Sauval (1998)
Opacities	OPAL Opacity (Iglesias & Rogers, 1996, updated 2001)
Low temperature opacities	(Alexander & Ferguson, 1994, updated 2005)
Equation of states	OPAL EOS (Rogers, Swenson, & Iglesias, 1996, updated 2006)
Core overshooting	Woo & Demarque (2001)

Opacities

ODF The opacity distribution function (ODF) as a non-grey treatment has been employed to our transfer problem (Kurucz, 1993). The key idea is that the transport of radiant energy can be calculated from the probability distribution of opacities composed of a series of rectangles.

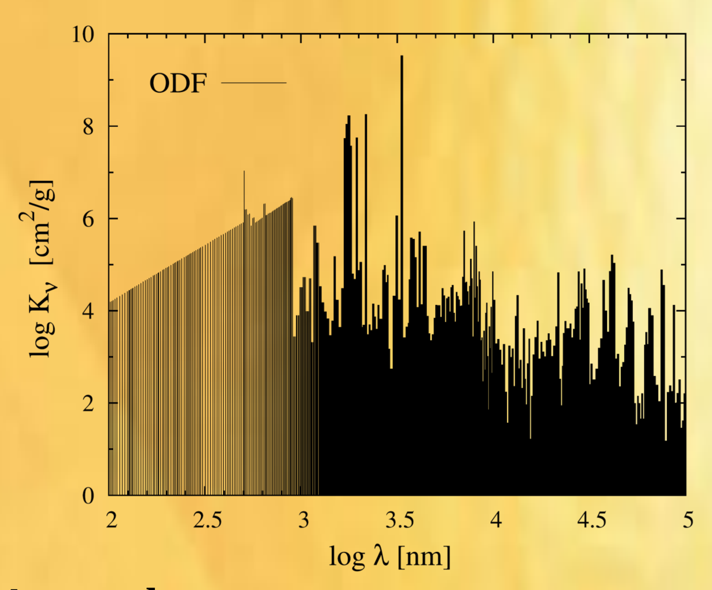

Grey Atmosphere The Rosseland mean opacity has been considered reasonable representation for grey opacity in deep layers. In this study, classical approximation such as grey atmosphere and Eddington approximation have been compared in 3-D HD computation.

$$\frac{1}{\kappa_{Ross}} \equiv \frac{\int_0^\infty \kappa_\nu^{-1}(\partial B_\nu/\partial T)d\nu}{\int_0^\infty (\partial B_\nu/\partial T)d\nu}$$

Model : (i) HD + ALI + ODF (ii) HD + EDD + ROSS

Hydrodynamics

Large-Eddy Simulation as a numerical tool for turbulent flows of stellar convection has been applied to a fully compressible Newtonian fluid. In order to describe stellar turbulent convection, the full set of Navier-Stokes equations should be solved.

$$\frac{\partial \rho}{\partial t} = -\nabla \cdot \rho \mathbf{v}$$

$$\frac{\partial \rho \mathbf{v}}{\partial t} = -\nabla \cdot \rho \mathbf{v}\mathbf{v} - \nabla P + \nabla \cdot \mathbf{\Sigma} + \rho \mathbf{g}$$

$$\frac{\partial E}{\partial t} = -\nabla \cdot [(E+P)\mathbf{v} - \mathbf{v} \cdot \mathbf{\Sigma} + f] + \rho \mathbf{v} \cdot \mathbf{g} + Q_{rad}$$

Domain is set to be a plain-parallel, closed box with stress-free top & bottom and periodic sides. Computational domain extends $4^2 \times 3$ Mm covering several granules and 8~9 pressure scale heights with the resolution of $117^2 \times 190$ staggered mesh grids (Chan & Wolff 1982). 3-D Snapshots has been accumulated during 800min in real time scale, which covers sufficiently the typical convective turn-over time.

Numerical Scheme consists of two steps : (i) An alternating direction implicit (ADI) with large time steps & first order accuracy and (ii) an explicit method (ADE) with second order accuracy. When the flow reaches statistical relaxation, simulation is switched to the explicit schemes incorporating the second order predictor-corrector time integration.

Simulations

Fig 1. Snapshots A horizontal slice **(top)** and a vertical slice **(bottom)** of the 3D thermodynamic structure are presented.

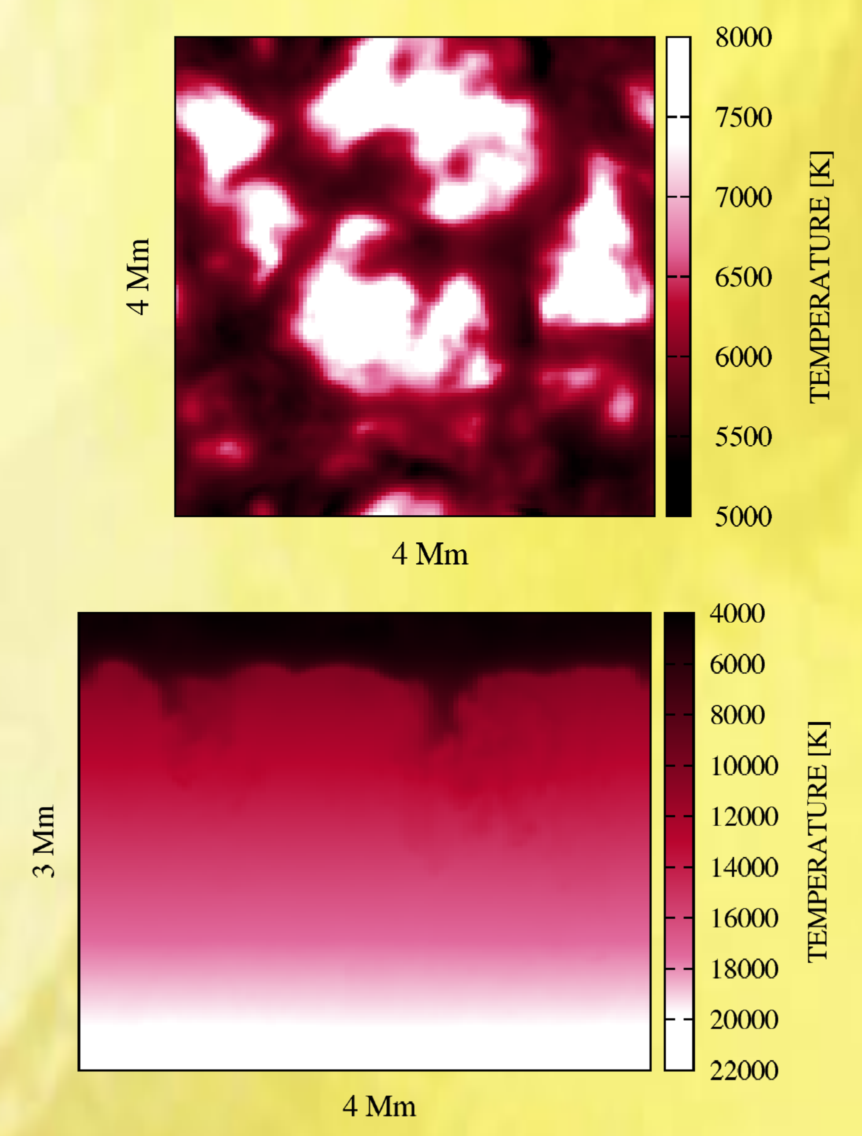

Radiative Transfer

ALI Accelerated Lambda Iteration method has been applied to 3-D HD medium as an optically thin regime ($\tau \le 10^4$).

$$J_\nu \equiv \Lambda_\nu S_\nu$$

$$\Lambda = \left(\Lambda - \Lambda^*\right) + \Lambda^*$$

$$J^{n+1} = \Lambda^*[S^{n+1}] + \left(\Lambda - \Lambda^*\right)[S^n]$$

$$S^{n+1} - S^n = [1-(1-\varepsilon)\Lambda^*]^{-1}[S^{FS} - S^n]$$

Eddington Approximation In previous version of RHD code, radiation part has been constructed using the generalized 3-D Eddington approximation as anisotropic diffusion in the upper region (Unno & Spiegel, 1966).

$$\nabla \circ \left(\frac{1}{3\kappa\rho}\nabla J\right) - \kappa\rho J + \kappa\rho B = 0$$

Diffusion In deep layers, the diffusion approximation has been considered as an optically thick regime ($\tau \ge 10^4$).

$$Q_{rad} = \nabla \cdot \left[\frac{4acT^3}{3\kappa\rho}\nabla T\right]$$

Fig 2. Radiation Fields **(top) The frequency averaged intensities near the solar surface.** The mean intensities are scaled by 1×10^{10} in cgs unit. **(bottom) Vertical distribution of mean intensity.** The frequency integrated mean intensities have been averaged temporally and spatially in computational domain.

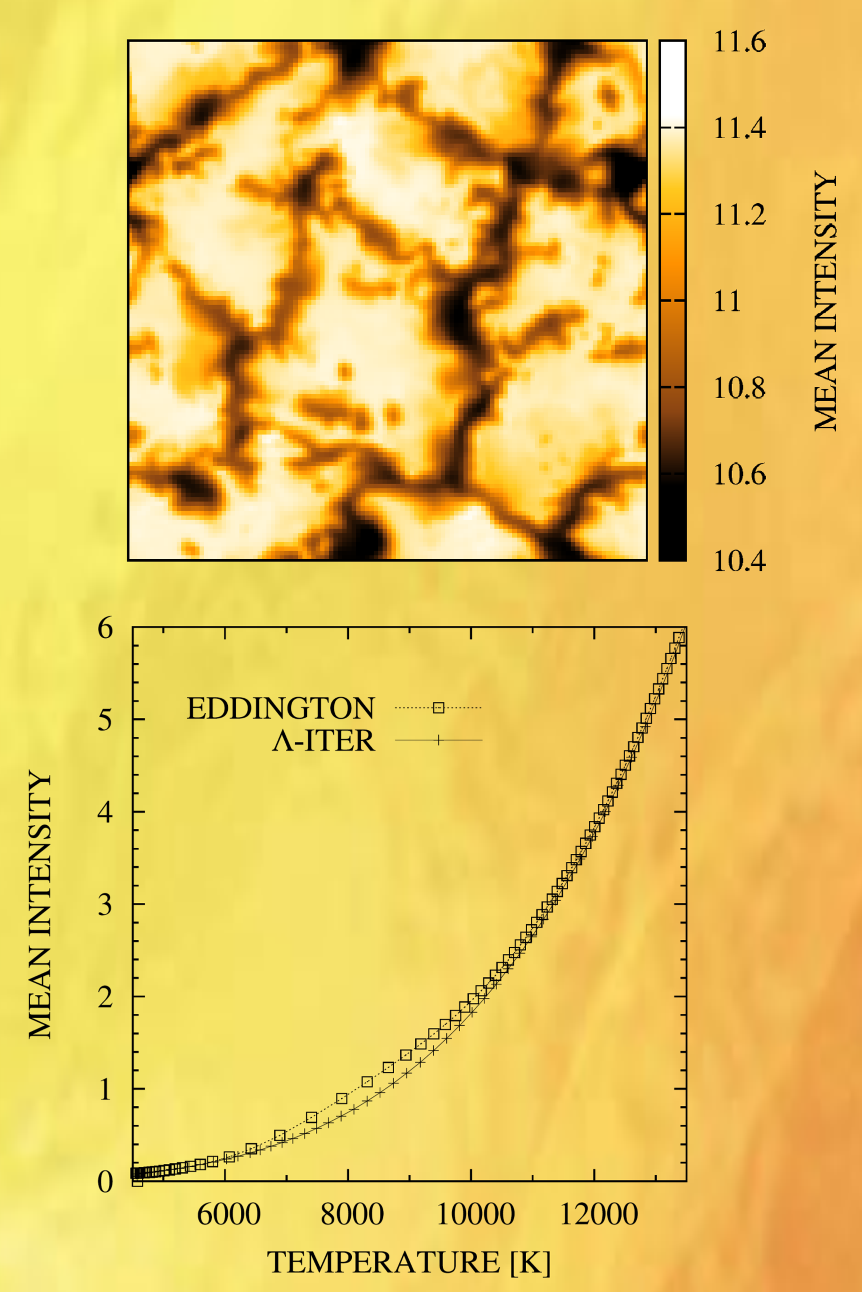

Discussion

The detailed radiative transfer schemes in the three dimensional hydrodynamical stellar surfaces are investigated. In order to describe radiation fields accurately, direct computation using the ALI method has been applied to the 3-D HD solar surface with a non-grey treatment of opacities. From our RHD simulation for the solar surface convection, thermodynamic structures including the topology and life time of the solar granules have been reconstructed. In surfaces and deep layers, the classical approximations are in a good agreement with the non-grey transfer computation. It implies that the Eddington approximation is a reasonable prescription approaching two limits : the streaming limit (τ ~ 0) and the diffusion limit ($\tau \gg 1$). However, there is a discrepancy of about 5% of radiant energy in the intermediate region of the super-adiabatic layers. The Rosseland mean underestimates the strength of absorbers in transition region. Now we are computing the other solar simulation incorporating the recent solar mixture (Asplund et al. 2009). We believe that a qualitative analysis of two simulations will provide better discrimination in the recent solar abundance problem. Convection and radiation are fundamental processes in the stellar astrophysics. Detailed information of radiation fields and thermodynamic properties from the direct numerical computation will provide deeper insight of physical processes in the Sun and stars.

ACKNOWLEDGEMENTS. This research was supported by ‘Yonsei-KASI Joint Research for the Frontiers of Astronomy and Space Science’ program funded by Korea Astronomy and Space Science Institute.

Progenitor for Type Ic Supernova 2007bi

Takashi Yoshida & Hideyuki Umeda

Department of Astronomy, Graduate School of Science, University of Tokyo

(Accepted for publication in MNRAS Letters; arXiv:1101.0635)

- **SN 2007bi** ➡ **~ 100 $M_\odot$ pair-instability supernova?** **or** **~ 40 $M_\odot$ core-collapse supernova?**

- **Evolution of very massive stars**

  $M_{MS} = 100 - 500\ M_\odot$

  $Z_0 = 0.004\ (= 0.2\ Z_\odot)$

  ➡ **CO core mass M_{CO}**

  Surface He abundance

  ➡ **Explosion mechanism?**

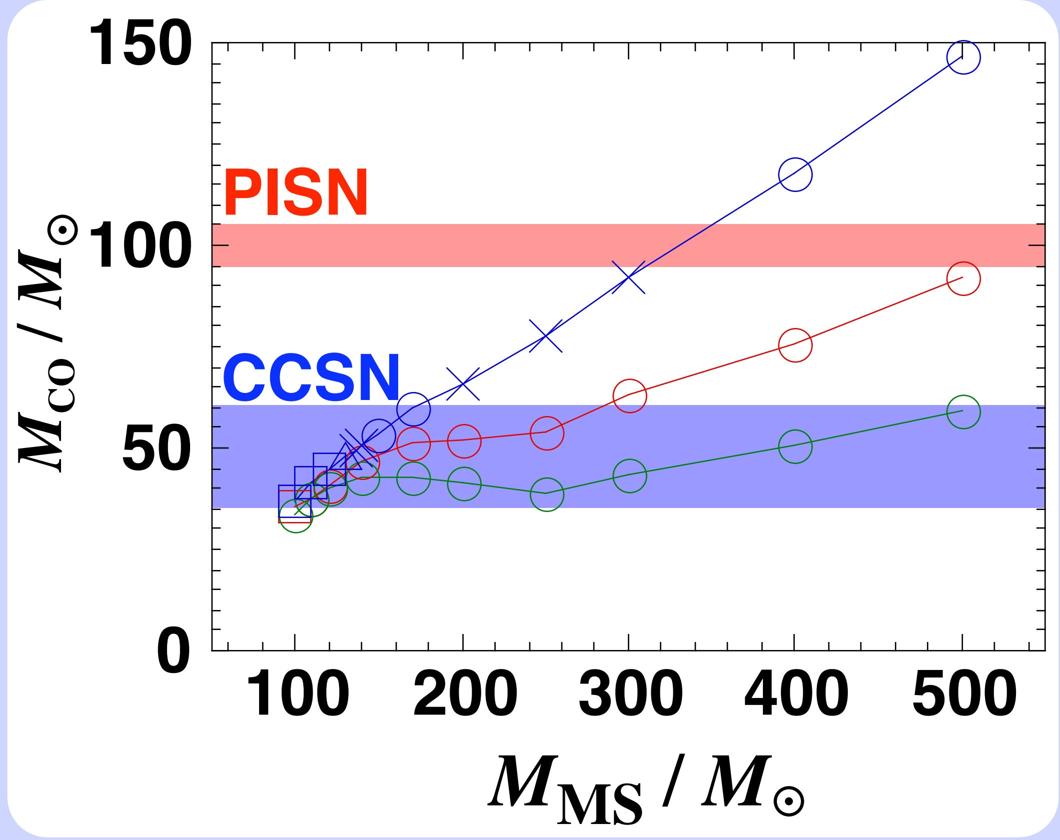

University of Leicester

Department of Physics and Astronomy

THE METAL CONTENT OF HOT WHITE DWARF SPECTRA

N. J. Dickinson*, M. A. Barstow, B. Y. Welsh, M. Burleigh, S. L. Casewell, J. Farihi, R. Lallement

*E-mail: njd15@le.ac.uk

- White dwarfs are evolutionary end products.
- Metals in cool white dwarfs; old planetary systems.
- Metals in hot white dwarfs; radiative levitation.
- Circumstellar metals near hot white dwarfs; also ancient planetary systems?

Analysis of CH_4 Q-branch absorption at 3.3μm in brown dwarf spectra with AKARI

Satoko Sorahana (The University of Tokyo, ISAS / JAXA)

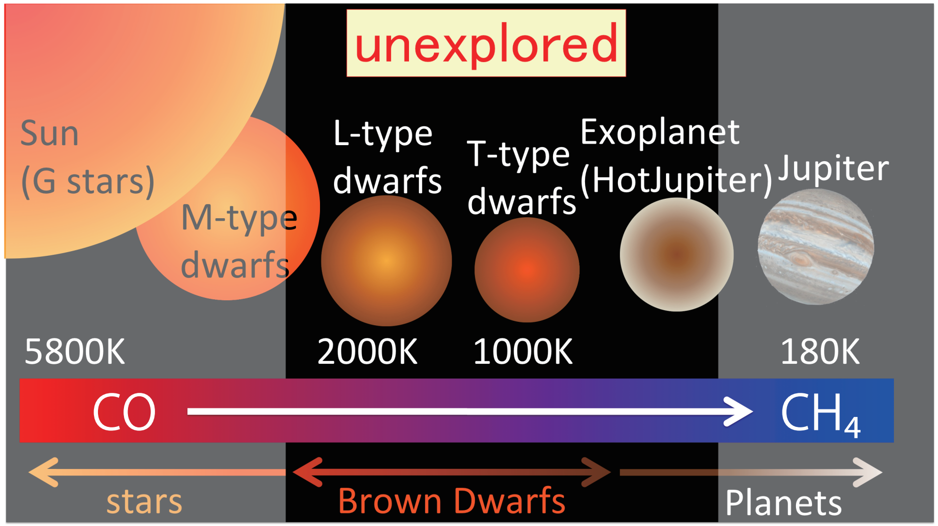

AKARI

a Japanese infrared astronomical satellite

- **Brown dwarfs** bridge between stars and planets.
- Carbon is transferred from CO to CH_4 as the temperature decreased.
- We can investigate how the atmosphere changes from stars to planets by CH_4 as a probe.

I'm studying how the CH_4 bands appears in brown dwarfs with AKARI.

Please come to see my poster

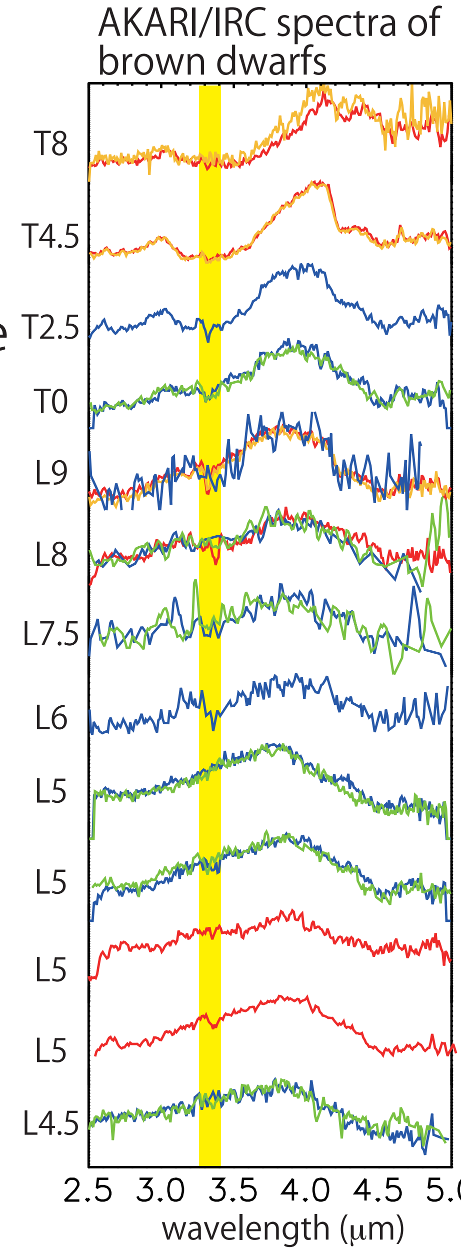

Boussinesq thermal convection in a rotating spherical shell with an outer stably stratified layer

Shin-ichi Takehiro, Michio Yamada and Yoshi-Yuki Hayashi

Configuration

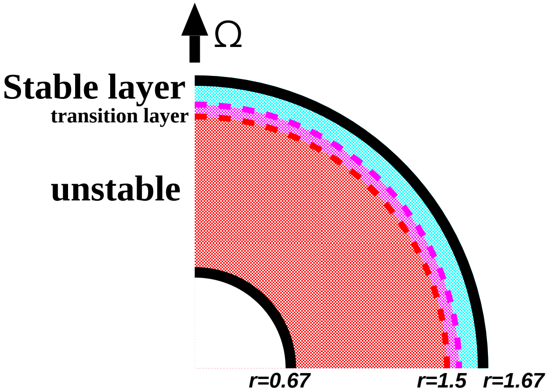

Mean zonal flows

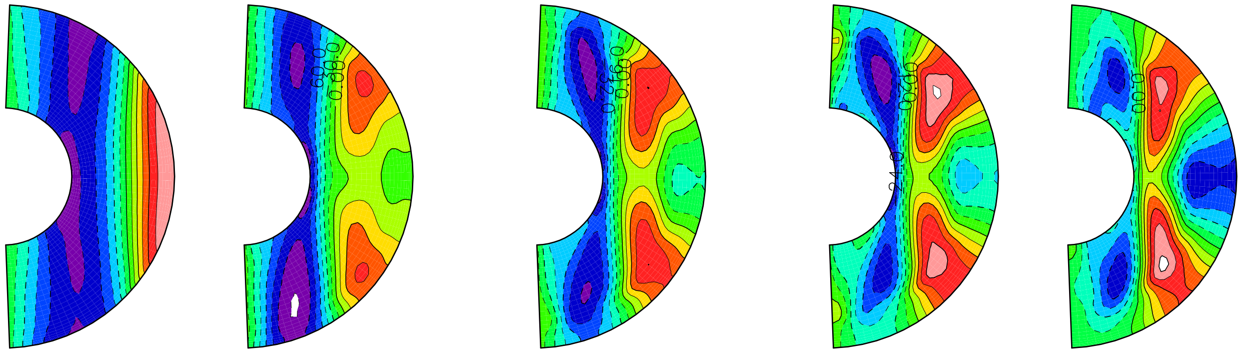

Weak ⟵ Stratification ⟶ Strong

- The existence of a strongly stratified upper layer enhances the generation of equatorial surface retrograde flows.

- The equatorial surface flows change from prograde to retrograde as the Rayleigh number is increased.

The Diffusion Induced Nova Scenario

Marcelo Miguel Miller Bertolami

Facultad de Ciencias Astronómicas y Geofísicas, Univ. Nac. de La Plata, Argentina

Instituto de Astrofísica La Plata, Unlp-Conicet, Argentina

Abstract

We propose a scenario for the formation of DA white dwarfs with very thin Helium buffers. For these stars we explore the possible occurrence of diffusion-induced CNO-flashes, during their early cooling stage. In order to obtain very thin helium buffers, we simulate the formation of low mass remnants through an AGB final/late thermal pulse (AFTP/LTP scenario). Then we calculate the consequent white dwarf cooling evolution by means of a consistent treatment of element diffusion and nuclear burning. Based on physically sounding white dwarf models, we find that the range of helium buffer masses for these diffusion-induced novas to occur is significantly smaller than that predicted by the only previous study of this scenario. As a matter of fact, we find that these flashes do occur only in some low-mass ($M < 0.6 M_\odot$) and low metallicity ($Z_{ZAMS} < 0.001$) remnants about $10^6 - 10^7$ yr after departing from the AGB. For these objects, we expect the luminosity to increase by about 4 orders of magnitude in less than a decade. We also show that diffusion-induced novas should display a very typical eruption lightcurve, with an increase of about 1 magnitude per year before reaching a maximum of $M_V \sim -5$ to -6. Our simulations show that surface abundances after the outburst are characterized by $\log N_H/N_{He} \sim 0.15...0.6$ and N>C>O by mass fractions. Contrary to previous speculations we show that these events are not recurrent and do not change substantially the final H-content of the cool (DA) white dwarf.

Introduction

Since the first simulations of white dwarf evolution that included a simultaneous treatment of diffusion and cooling (i.e. Iben & MacDonald 1985, 1986) it was noticed that diffusion could trigger thermonuclear CNO-flashes. In fact, the inward diffusion of H and the outward diffusion of C within the pure He zone (usually named "He-buffer", see Fig. 1) left after the last thermal pulse can lead to a runaway CNO-burning. This produces a very rapid expansion, of the order of years, of the outer layers of the white dwarf pushing the star back to a giant configuration and increasing its visual magnitude from $M_V \sim 9$ to $M_V \sim -6$ in a few years. We term this eruptive event as "diffusion-induced nova" (DIN) although it leads to a much slower brightening than classical novas. Iben & MacDonald (1986) showed that after such events the stars will become, in a few years, yellow giants with mildly He enriched surface compositions. In a more speculative mood they also suggested that DINs may be recurrent, finally leading to H-deficient compositions. Later, prompted by this speculation, D'Antona & Mazzitelli (1990) suggested that the H-rich envelope could be strongly reduced during these events, leading to DA white dwarfs with thin H-envelopes, as inferred in some DA white dwarfs (Castanheira & Kepler2009).

The main purpose of the present work is to study the possibility that DINs could take place in physically sounding white dwarf models with a realistic evolutionary history. We will also identify a detailed scenario for the creation of white dwarfs with thin enough He-buffers for DIN events to occur. Specifically, to perform this study we compute realistic white dwarf models by means of "cradle to grave" stellar evolution simulations. Then we compute white dwarf cooling sequences by considering a simultaneous treatment of element diffusion and evolution.

Brief description of the stellar evolution code

White dwarf models are obtained as the result of computing the evolution of low mass stars from the ZAMS through the helium core flash and through the thermal pulses on the AGB (TP-AGB) and, then, to the white dwarfs stage. LPCODE considers a simultaneous treatment of non-instantaneous mixing and burning of elements, by means of a diffusion picture of convection coupled to nuclear burning —see Althaus et al. (2005) for numerical procedures. The nuclear network considered in the present work accounts explicitly for the following 16 elements: ^{1}H, ^{2}H, ^{3}He, ^{4}He, ^{7}Li, ^{7}Be, ^{12}C, ^{13}C, ^{14}N, ^{15}N, ^{16}O, ^{17}O, ^{18}O, ^{19}F, ^{20}Ne and ^{22}Ne, together with 34 thermonuclear reaction rates corresponding to the pp-chains, the CNO bi-cycle, He-burning and C-ignition as described in Miller Bertolami et al. (2006).

The treatment of diffusion is similar to that of Iben & MacDonald (1985, 1986) but we consider, in addition gravitational settling and chemical diffusion, the process of thermal diffusion. We do not take into account radiative levitation, as it is only relevant for determining surface chemical abundances and, thus, is irrelevant for the purpose of the present work. Our treatment of time dependent element diffusion is based on the multicomponent gas picture of Burgers (1969). Specifically, we solved the diffusion equations within the numerical scheme described in Althaus et al. (2003).

The proposed evolutionary scenario

Whether white dwarfs with thin He-buffer can be actually formed relies on identifying a scenario in which they could be formed under standard assumptions. As shown in Fig. 1, after a He-shell flash on the TP-AGB, the mass of the He-buffer region becomes strongly reduced by intershell convection. Such thin He-buffer survives until the reignition of the H-burning shell.

In particular, the first thermal pulses of low-mass stars ($M \sim < 1.5 M_\odot$) are not very strong and, thus, no third dredge up takes place in numerical models. Hence, it is not unreasonable to accept that low-mass stars experiencing an AGB final thermal pulse (AFTP) or a Late Thermal Pulse (LTP) will end as DA white dwarfs with thin He-buffers. In those cases, as no third dredge up happens, the very thin He-buffer survives the last helium shell flash (either AFTP or LTP). Then, during the He-burning phase that follows the flash, AGB winds will erode an important fraction of the remaining (already depleted) H-rich envelope, preventing a reignition of the H-burning shell and an increase in the He buffer mass. As a result, the He-buffer is still very thin when the star finally reaches the white dwarf phase. Then, when the star enters the white dwarf cooling phase, the inward diffusion of H and the outward diffusion of C within the He-buffer leads to the ignition of a CNO-burning shell and ultimately to a CNO-flash (see Fig. 2).

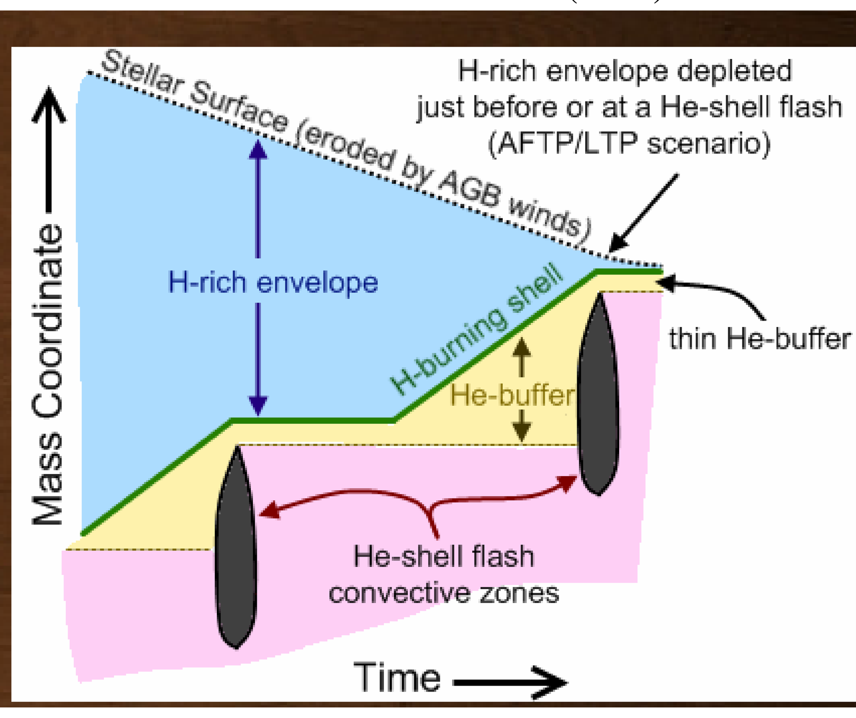

Figure 1. Sketch of a Kippenhahn diagram of the proposed sce nario for the formation of DA white dwarfs with thin He-buffers.

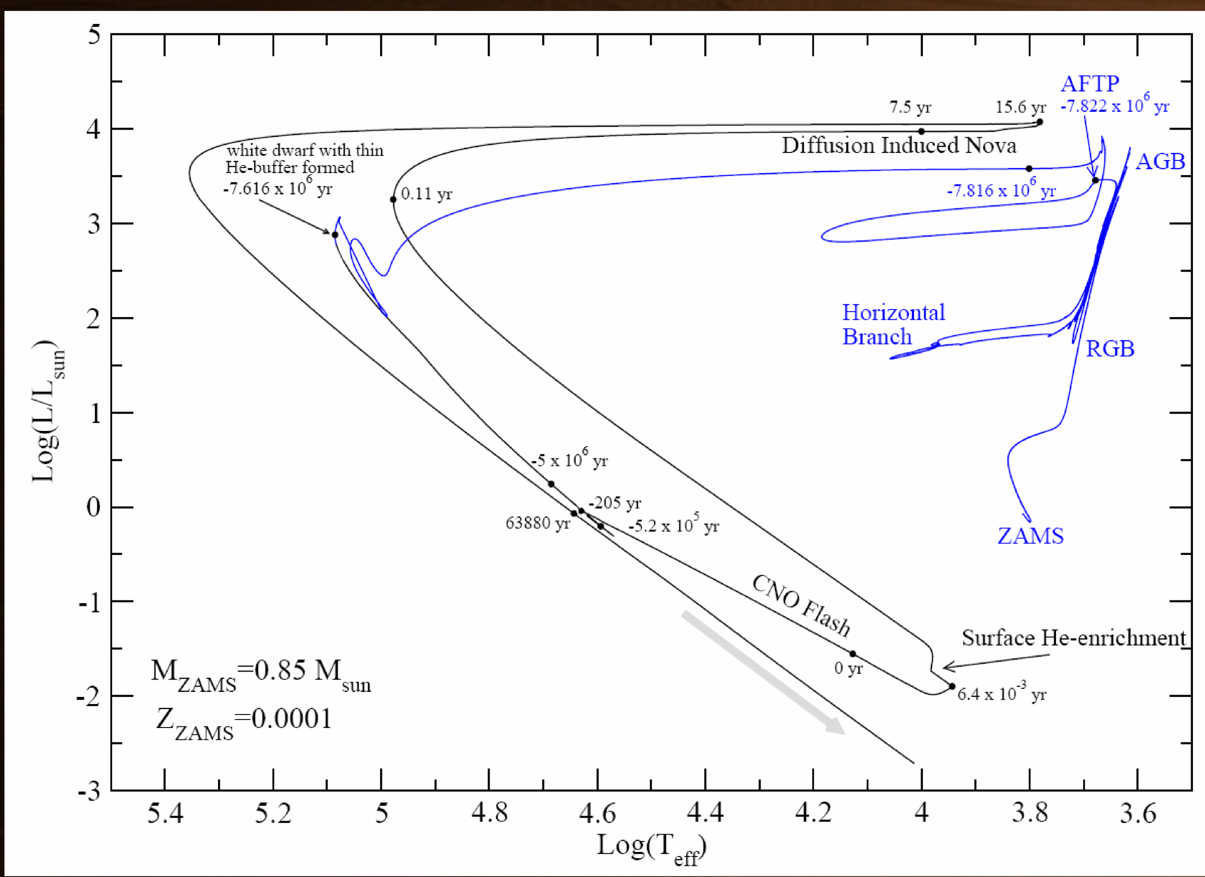

Figure 2. Evolutionary track in the HR-diagram of one of our DIN-sequences (M_{WD}=0.53946 $M_\odot$, see Table for more details). The blue part of the curve describes the pre-white dwarf evolution. Note the last thermal pulse during the departure from the AGB (AFTP, blue loop) which leads to the formation of a thin He-buffer in the white dwarf as described in Fig. 1. The black curve shows the evolution during the white dwarf stage and the diffusion induced nova event. Black dots indicate the time before and after the maximum energy release during the CNO-flash. Note that, after the CNO-flash the star acquires a giant configuration in only 15 yr. This violent change in the luminosity and temperature of the star leads to a very characteristic visual lightcurve for these objects (see Fig. 3).

As a consequence of convective mixing of the pure H envelope with material from the He-buffer the surface abundances of the star during the outburst are strongly enriched in He and N (see Table).

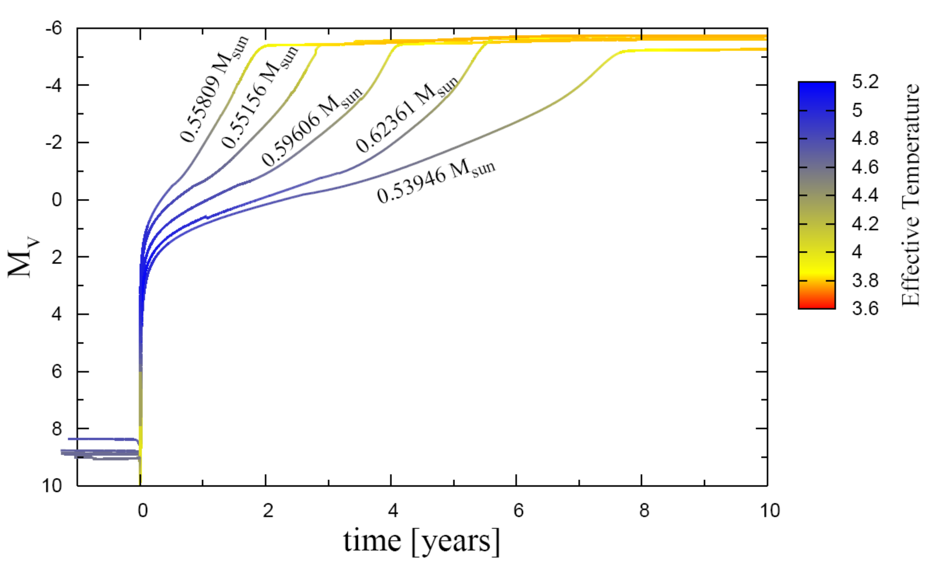

Figure 3. Predicted lightcurves and temperatures for our DIN simulated sequences during the outburst.

Progenitor Mass	White Dwarf Mass	$\log L_{pre}/L_\odot$	$\log T_{eff}^{pre}$	τ_1 [yr]	τ_2 [yr]	$\lvert dM_V/dt \rvert$	τ_3 [yr]	τ_4 [yr]	H	He	C	N	O
$0.85M_\odot$	$0.53946M_\odot$	-0.31	4.57	7.6×10^6	7.9	1.6	260	$\lesssim 1.6\times10^5$	0.39	0.61	10^{-5}	2.2×10^{-4}	1.1×10^{-6}
$0.85M_\odot$	$0.54006M_\odot$†	-0.46	4.54	1.2×10^7	10.2	1.3	-	-	0.28	0.72	4×10^{-6}	6.1×10^{-5}	3.6×10^{-7}
$0.85M_\odot$	$0.54076M_\odot$†	-0.96	4.42	4×10^7	4.9	1.6	-	-	0.19	0.81	10^{-5}	1.4×10^{-4}	10^{-6}
$0.85M_\odot$	$0.54115M_\odot$†	-1.19	4.37	7.7×10^7	2.7	2.4	-	-	0.15	0.85	4×10^{-5}	3.3×10^{-4}	3.2×10^{-6}
$1M_\odot$	$0.55156M_\odot$	-0.33	4.57	6.5×10^6	3	3.3	270	9.7×10^4	0.38	0.62	2×10^{-4}	4.2×10^{-3}	10^{-6}
$1.25M_\odot$	$0.59606M_\odot$	-0.05	4.65	3.4×10^6	4.2	2.9	216	5.5×10^4	0.49	0.51	5×10^{-5}	1.3×10^{-3}	10^{-5}
$1.8M_\odot$	$0.62361M_\odot$‡	0.25	4.73	2.2×10^6	5.7	2.7	49	3.1×10^4	0.46	0.54	2×10^{-5}	4.6×10^{-3}	3×10^{-6}
$1.M_\odot (Z=0.001)$	$0.55809M_\odot$	-0.47	4.54	8.9×10^6	2.1	3.9	456	1.1×10^5	0.30	0.70	1×10^{-4}	1.9×10^{-3}	4×10^{-6}
$0.85M_\odot$	$0.53946M_\odot$(w/OV)≀	-0.31	4.57	7.6×10^6	0.66	6.2	1367	5.2×10^4	0.22	0.73	6.6×10^{-3}	0.038	1.1×10^{-3}
$0.85M_\odot$	$0.53946M_\odot$(w/OV, CO-rich)≀,∗	-0.03	4.63	4.1×10^6	0.42	3.1	1628	5.8×10^4	0.23	0.62	0.033	0.081	0.033
IM86 $(Z=0.001)$	$0.6M_\odot$	-0.54	4.52	$\sim 10^7$	~ 7.5	-	-	-	0.29	0.71	6.6×10^{-4}	7.5×10^{-4}	8.1×10^{-6}

Table Outburst properties of the DINs studied in this work. With exception of the last sequence all sequences come from ZAMS progenitos with $Z = 0.0001$. Timescales are defined as follows; cooling time at the moment of the CNO-flash (τ_1), expansion time from the maximum energy release to the giant stage at $\log T_{eff} = 3.9$ (τ_2), duration of the cool ($\log T_{eff} < 4$) giant stage (τ_3) and contraction time needed to reach the pre-outburst luminosity (τ_4). †These remnants were obtained by reducing the mass lost during the final AGB thermal pulse from that predicted by standard AGB wind prescriptions. ‡This remnant was obtained by applying an artificially high wind during the fifth thermal pulse.≀ These DINs were obtained form the $0.53946M_\odot$ sequence by including OV in the convective zone generated during the CNO-flash. ∗ In this case the intershell composition of the remnant was modified to resemble the C- and O- rich surface abundances of PG1159 stars.

Results

- We have identified a definite scenario leading to the formation of DA white dwarfs with thin He-buffers. Such white dwarfs are naturally formed in low-mass stars, that do not experience third dredge up during the TP-AGB, and suffer from either an AFTP or a LTP.
- We have explored the parameter space of the DIN scenario and shown that there is a range of values of $M_\star$, Z_{ZAMS} and He-buffer masses for which DIN occur in physically sounding white dwarf models. Our results suggest that DINs take place in white dwarfs with $M_\star < 0.6$ and $Z_{ZAMS} < 0.001$ and thin He-buffers —as those provided by the scenario described above.
- Our simulations provide a very detailed description of the events before, during and after the DIN event. In particular, our results show that DIN events are not recurrent as previously speculated. Thus, DINs do not form H-deficient white dwarfs, nor DA white dwarfs with thin H-envelopes.
- We have qualitatively described the mechanism by which the CNO-shell becomes unstable. Our analysis shows that the occurrence of CNO-flashes depends strongly on the intensity of the CNO-burning shell (as compared to the core luminosity), and its temperature. This seems to be in agreement with the fact that only our sequences with $M_\star < 0.6$ and $Z_{ZAMS} < 0.001$ and thin He-buffers experienced DIN events.
- Regarding the criterion presented by Iben & MacDonald (1986) for the occurrence of DIN events, we find that such criterion is misleading as the He-buffer mass is not the only parameter that determines whether a DIN event will take place or not. In particular, for more massive remnants our simulations do not predict DIN for any possible He-buffer masses.
- Our simulations provide a very detailed description of the expected surface abundances and lightcurves during the outbursts. In particular we find that typical lightcurves display a maximum of $M_V \sim -5.5$, a brightness speed of a few magnitudes per year, and a mild He- and N- enrichment; with $N \sim 10^{-4} - 10^{-3}$ by mass fraction and $\log N_H/N_{He} \sim$ -0.15...0.6. Also, in all our sequences we find surfaces abundances with N > C > O by mass fraction.
- We find that the inclusion of extramixing events at the boundaries of the CNO-flash driven convective zone leads to higher He, N, C and O abundances than in the case in which no extramixing is considered. Relative surface CNO abundances in these cases are N > C > O (by mass fractions), although the precise values will be strongly dependent on the C and O composition of the He-, C- and O- rich intershell.

Mass Loss of Massive RSGs

ZAMS mass range of Type IIP SN progenitor (RSGs)

<Minimum>

~ 8 Msun

<Maximum>

- Theoretically ~ 25 Msun
- Observationally ~ 17 Msun

→ Mass loss of massive RSGs?

UV-bright Type IIP SN 2009kf

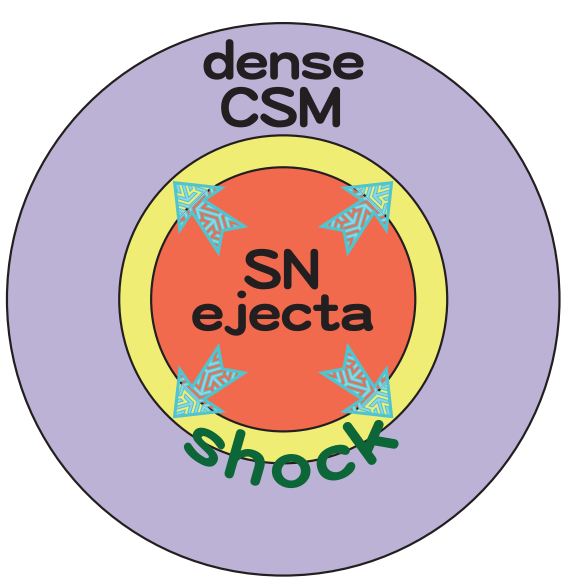

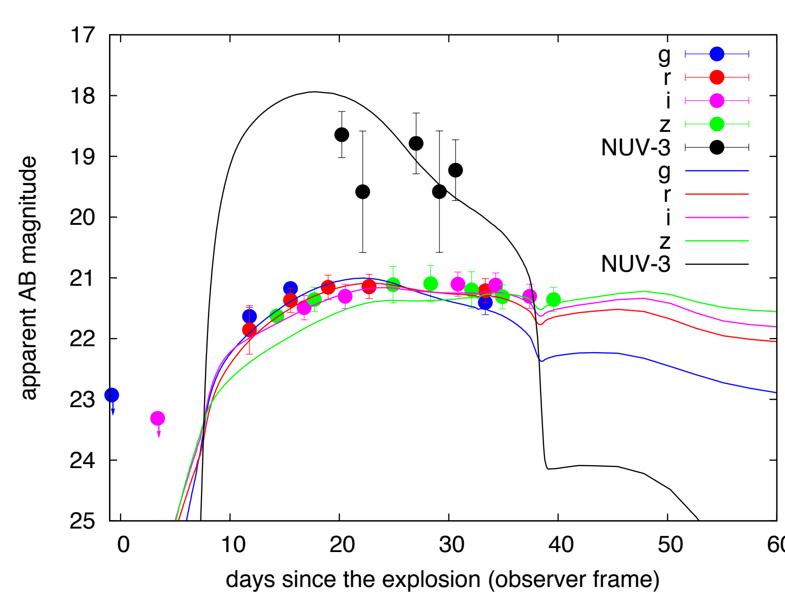

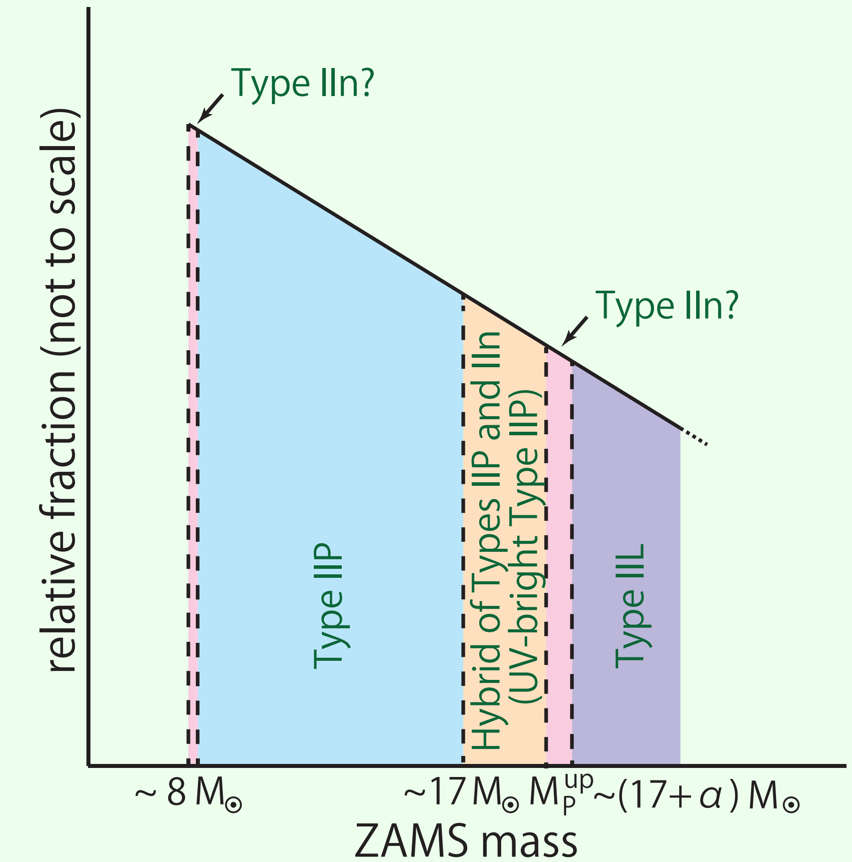

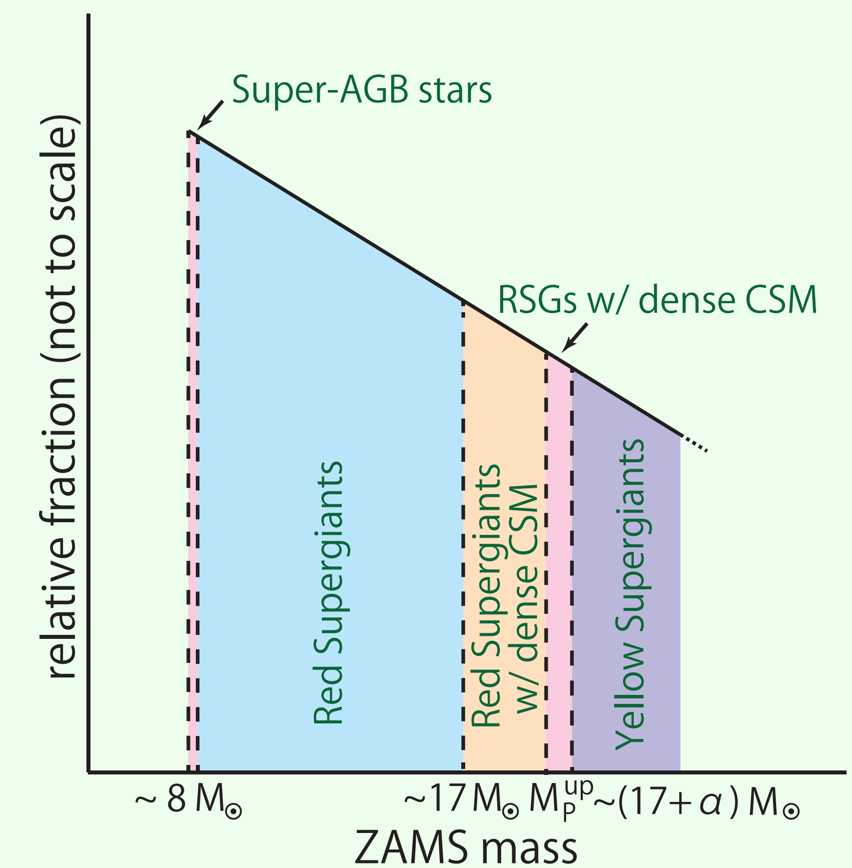

Polarimetry of Earthshine as a Test of Ocean Detection on Exoplanets

J. Takahashi, Y. Itoh (Kobe-U/CPS), T. Niwa (NHAO), and Y. Hirowatari

- Specular reflection on smooth liquid surface on a planet will cause a great polarized fraction in the total reflected light (McCullough 2006, Zugger+ 2010).
  - Detectable difference between "land planets" and "ocean planets"?
- Earthshine observed from Japan:
  - Waxing Moon = from a continent-dominant surface
  - Waning Moon = from an ocean-dominant surface
- We conduct imaging polarimetry of Earthshine with 60 cm reflector at NHAO.

*1

*2

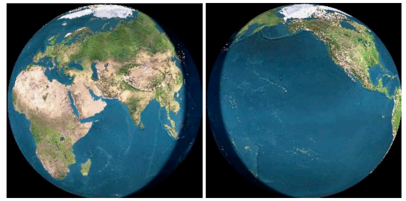

Obtained image ▶

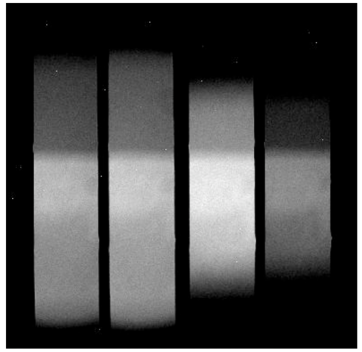

Phase curves ▼

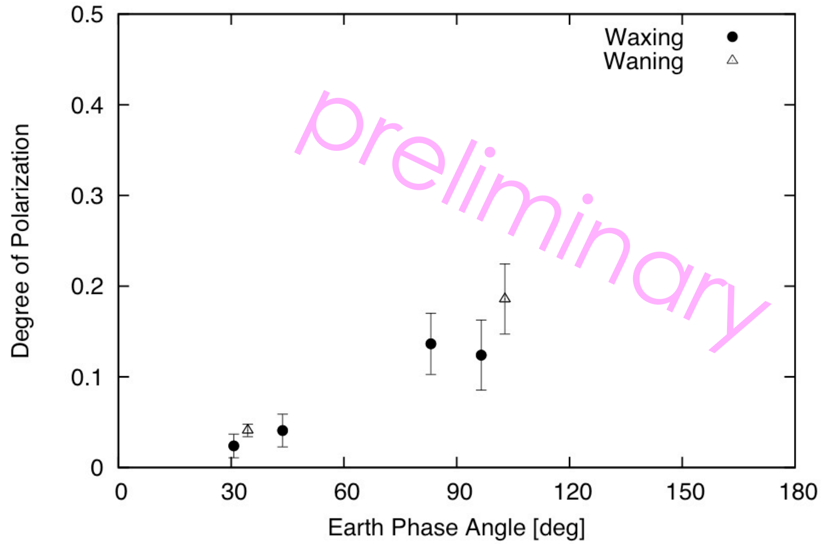

(1) http://www.f3.dion.ne.jp/~p2k/moon.html

(2) Generated by Earth and Moon Viewer: http://www.fourmilab.ch/earthview/vplanet.html

Dry minor mergers and size evolution of early-type galaxies in high density environments

Taira Oogi (Hokkaido University)

- To study size evolution of early-type galaxies, we simulate dry major and minor mergers between early-type galaxies with N-body simulations.
- Our results indicate that minor mergers, in particular continuous ones are very efficient way to size evolution of ETGs.

Continuous minor mergers

Synchronized minor mergers

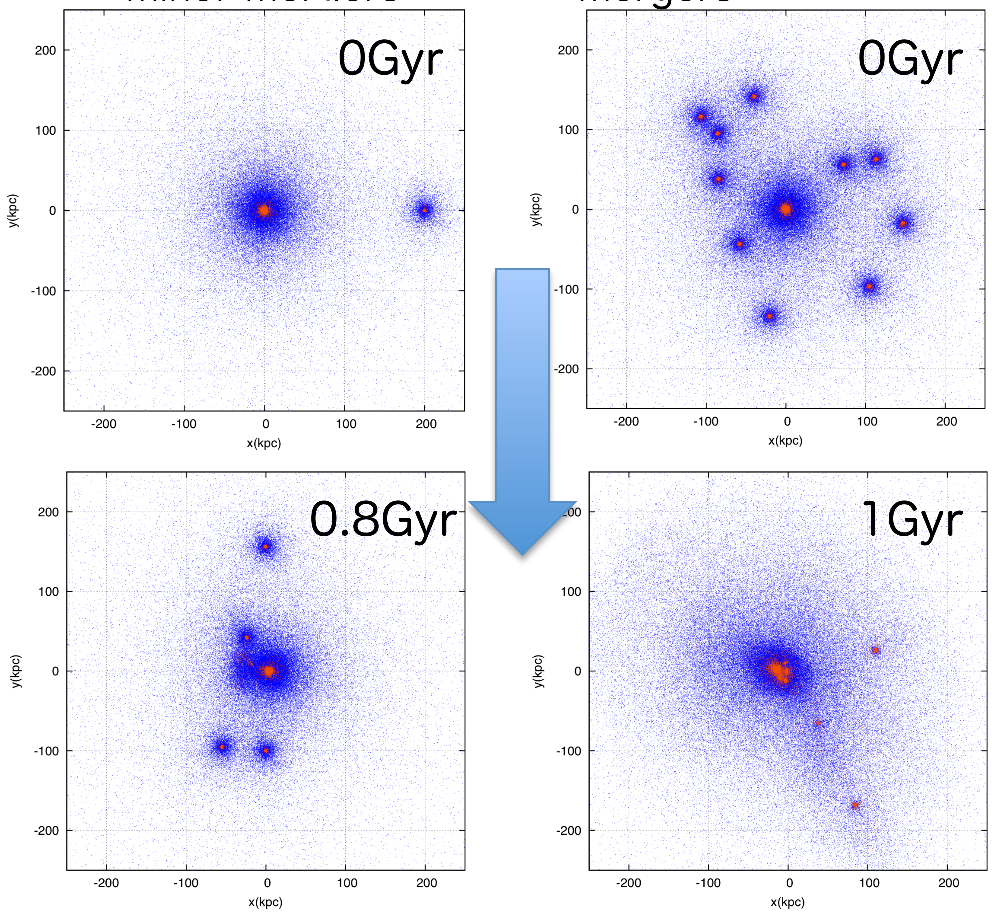

Merger remnant's density profile

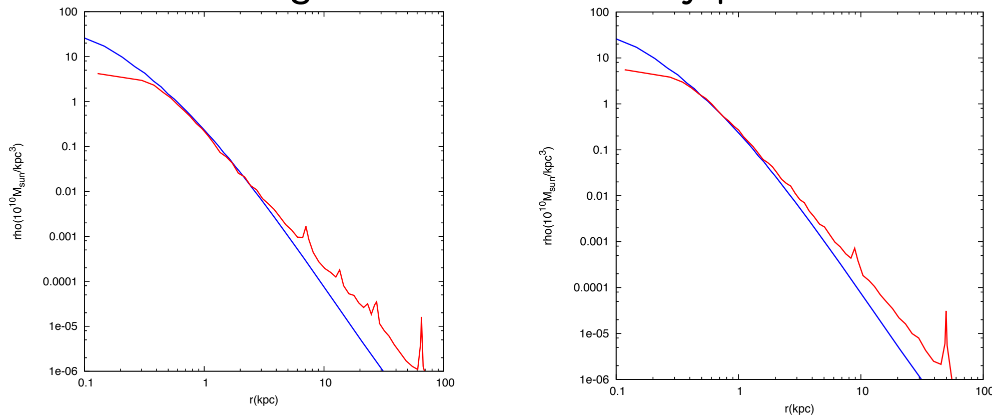

Galaxy stellar mass-size plane

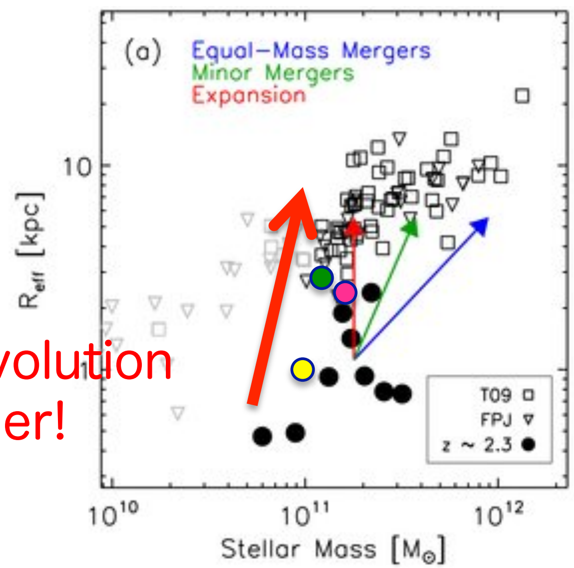

Path of size evolution by minor merger!

The Relation between the Stellar Structure of Red Giants and the Formation and Evolution of Gas Giant Planets

Kazuhiro Kanagawa (Hokkaido University)

◆ Similarity between Red Giants and Gas Planet

- ✓ Red giant have structure composed by collapsing core and expanding envelope
- ✓ Gas Planet have structure composed by solid core and gaseous envelope

➡

- ➢ **Gas Giant Planet should have Core-Halo Structure**
- ➢ **It's behavior can be understood by double-polytrop model.**

◆ Difference between Red Giants and Gas Planet ➡ Outer boundary condition

- ✓Surface thermal condition of Gas Planet is fixed as disk condition.
- ✓Red Giant have zero boundary condition.

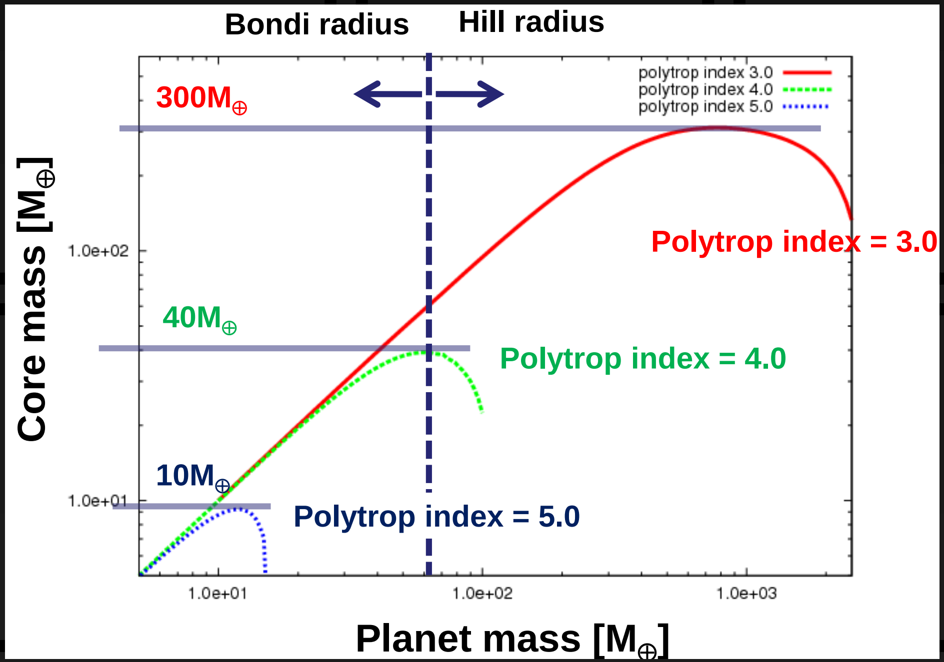

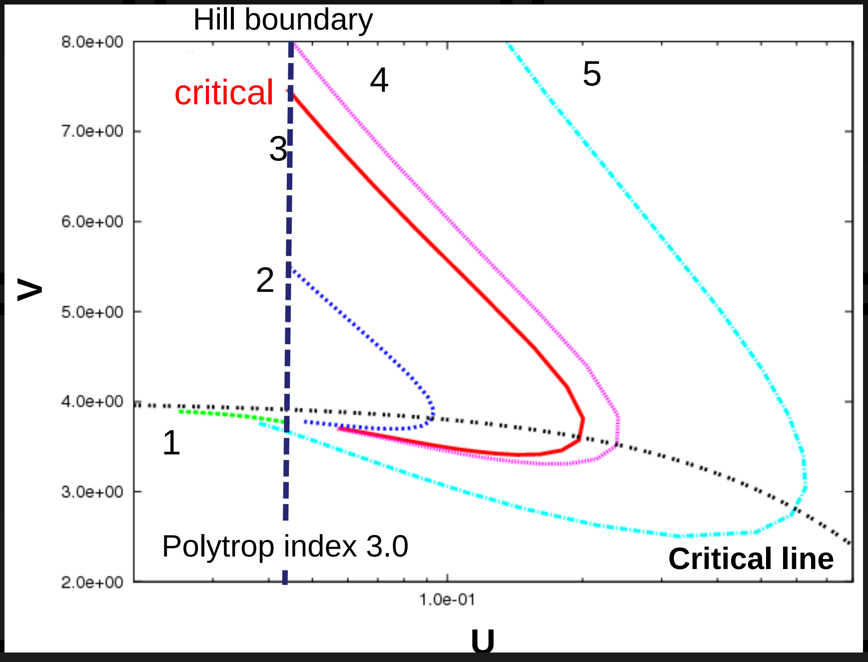

Lithium depletion in solar-like stars: no planet connection

- Sample of 117 solar-like stars (i.e. mass, metallicity, surface gravity)
- Precise stellar parameters and surface lithium abundances
- We find strong evidence for lithium depletion with age
- Compare results with claims for stronger lithium depletion in planet hosts

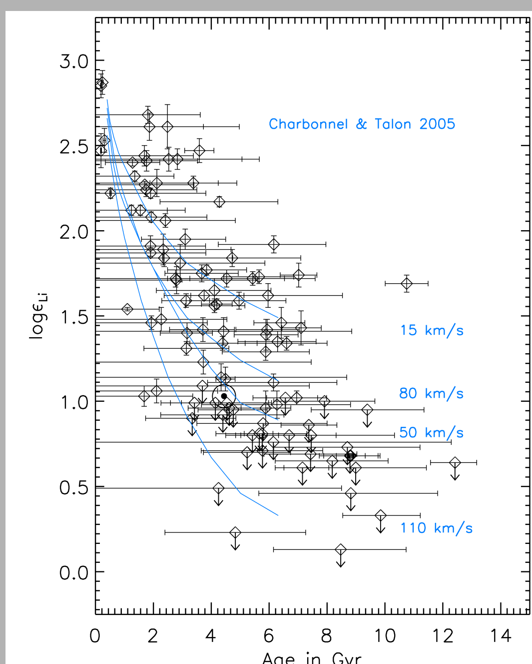

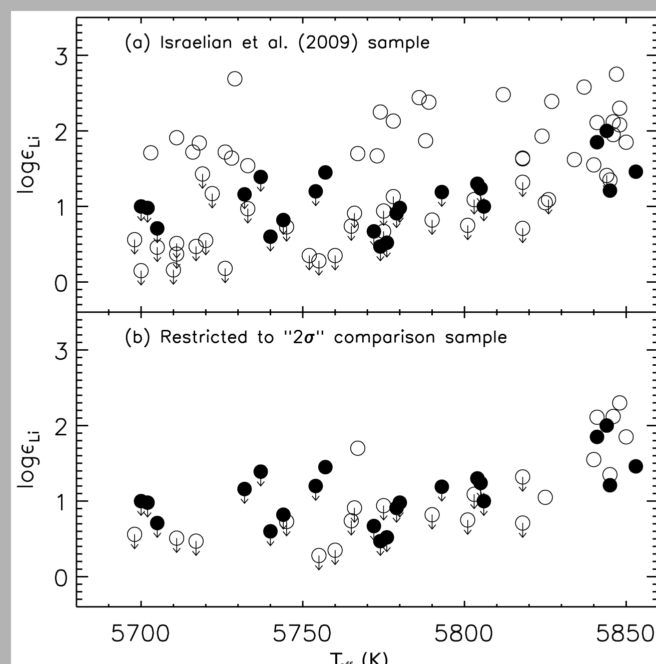

"Extra finding":
Some stars have very high log ε_{Li} for their ages. Those appear to be sub-giants.
→ Dredge-up at the end of the main sequence?

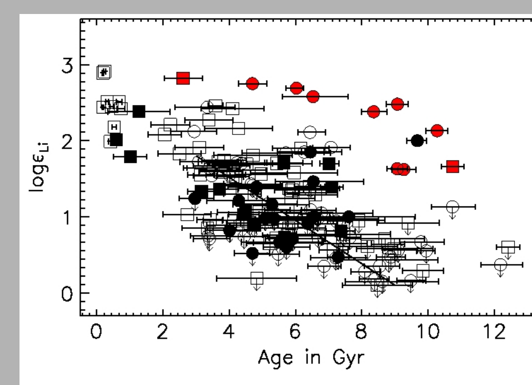

Patrick Baumann, Max Planck Institute for Astrophysics, Garching, Germany